

5. STRUCTURAL RESPONSE

5.1 Finite Element Calculations for Impacts onto Rigid Targets

5.1.1 Introduction

To determine the response of the generic casks, finite element calculations for impacts onto rigid targets were conducted. For all of the analyses in this report, the Sandia-developed non-linear transient dynamics finite element program PRONTO-3D [5-1, 5-2, 5-3] was used to determine the damage resulting from each impact. PRONTO is a shock-wave propagation code, especially developed for impact problem types. It uses a time marching explicit integration of the equation of motion to determine the response of the structure. Inputs to the code are geometry (including boundary conditions), material properties, and initial velocities. This type of code updates the position of each node at each time step, which allows for both material and geometric non-linearities. One result of this approach is that strains reported are true strains, rather than engineering strains that are based upon the undeformed geometry. PRONTO has been extensively benchmarked for analyses of cask response [5-4, 5-5]. For each generic cask, calculations were performed for impacts in end-on, CG-over-corner, and side-on orientations. The response of the casks at other orientations is sufficiently similar to (or bounded by) these results to be enveloped by them. For impact angles between end-on and 5 degrees from vertical, the end-on analysis results will be used. For impacts between 5 degrees from vertical to 70 degrees from vertical the CG-over-corner analysis results will be used. For impacts between 70 degrees from vertical to horizontal, the side-on analysis results will be used. All impacts are assumed to be onto a flat, rigid surface with the initial velocity perpendicular to the surface. While it is possible for a cask to impact a surface that is not flat (such as a bridge column) in a side impact orientation (such that the contact occurs between the impact limiters), this type of accident was not considered. An impact of this type only provides loading and, therefore, deformation to the cylindrical portion of the cask away from the closure area. This part of the cask is extremely ductile, and can withstand deformations greater than the cask diameter without causing the cask to release radioactive material.

To shorten the analysis times and avoid calculation of the very large shear strains that occur in the impact limiter, at the start of all of the analyses it was assumed that the impact limiter has already been driven into the lock-up region (the point at which the material stops behaving in a crushable manner). The initial and crushed size of the impact limiters for each cask are given in Table 5.1. Figure 5.1 shows the initial and pre-crushed geometry of an impact limiter. The amount of energy absorbed by the impact limiter prior to lock-up is equivalent to the kinetic energy from the regulatory drop test. Using the pre-crushed impact limiter, analyses with impact velocities of 30, 60, 90, and 120 mph are conducted for each cask and orientation. If the energy required to crush the impact limiters is added to the initial kinetic energy of the cask, these analysis velocities correspond to actual impact velocities of 42, 67, 95, and 124 mph. However, throughout this report the calculations will be identified as 30, 60, 90, and 120 mph impact cases.

Table 5.1 Impact Limiter Geometry (in inches)

Cask	Cask Diameter	Engagement Length	Initial End Thickness	Crushed End Thickness	Initial Side Thickness	Crushed Side Thickness
Steel-Lead-Steel Truck	27.5	12	12	4	12	4
Steel-DU-Steel Truck	28	12	12	4	12	4
Steel-Lead-Steel Rail	80	14	14	4.67	14	4.67
Monolithic Rail	85	14	14	4.67	14	4.67

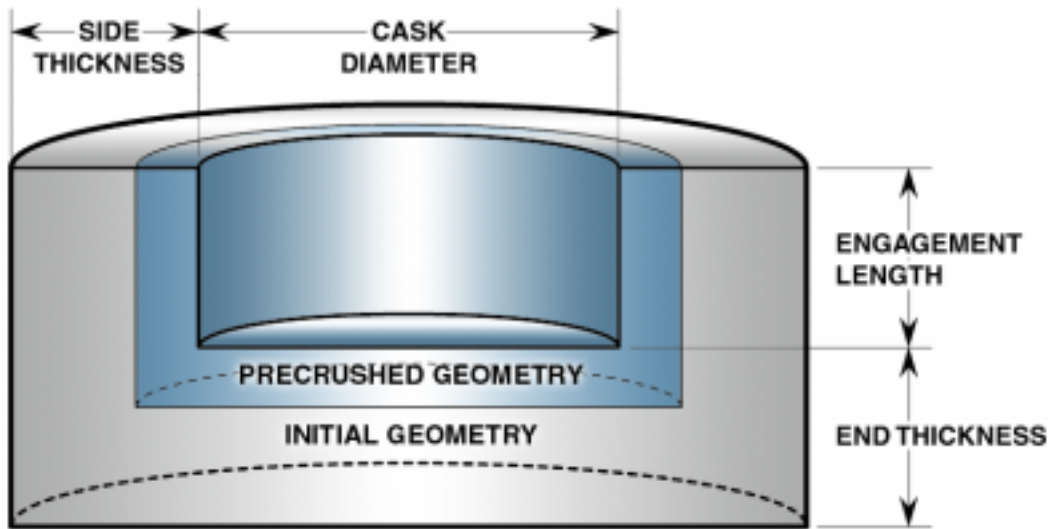


Figure 5.1 Geometry of the initial and pre-crushed impact limiter.

5.1.2 Assumptions for Finite Element Models

While it is possible to create a finite element mesh that accurately models all of the details of the generic cask models, using these models requires too much computation time for the many cases considered in this work. For this reason, simplifying assumptions were made. All of the impacts considered have a plane of symmetry through the long axis of the cask, so it is only necessary to model one-half of the structure. Figure 5.2 shows the finite element model used for the lead shielded rail cask, typical of the models used for all of these analyses.

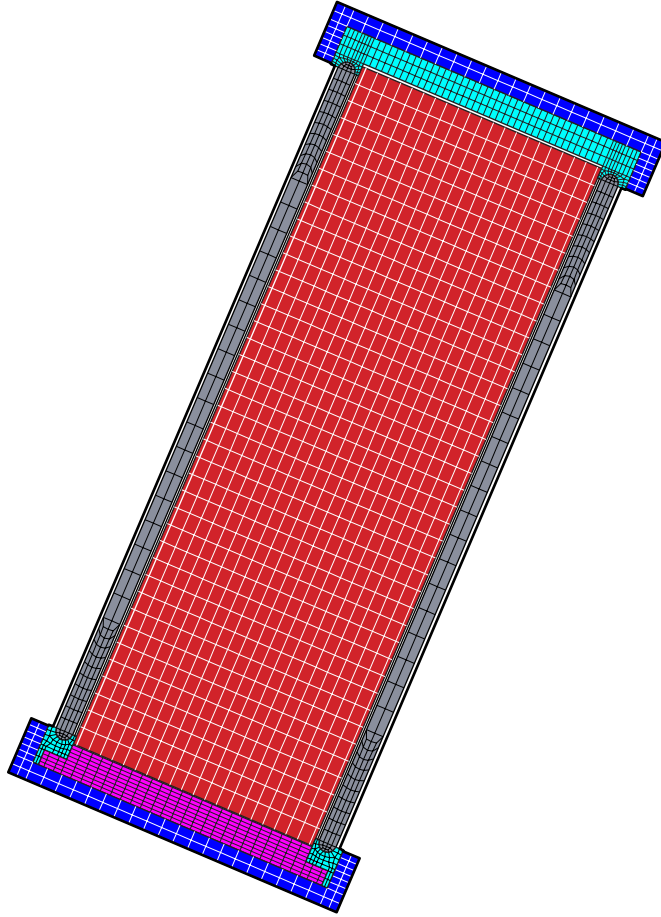


Figure 5.2 Finite element model of the steel-lead-steel rail cask in the CG-over-corner drop orientation.

For all of the sandwich-wall casks the inner and outer steel layers were modeled with zero-thickness shell elements. This type of element accurately captures the bending behavior and axial forces in the shell, but does not incorporate stresses in the direction perpendicular to the shell surface. Where this fact has the greatest influence is in the contact between the various layers. If the geometry of the contents and shielding layer are modeled correctly, it is impossible for a zero-thickness shell element to be contacting both the contents and the shielding. In these finite element models the shell elements are located at the mid-thickness of the wall layer they represent. This leaves a gap between the contents and the shell and between the gamma shielding and the shell. The gap between the contents and the shell is typical of spent fuel casks, but the gap between the gamma shielding and the shells results in having the gamma shielding (and the shells) unsupported for motion in the direction transverse to the shells. This results in larger deflections and strains in the sandwich wall for the model than would occur in reality. For casks with lead gamma shielding the lack of lateral support results in a significant over-prediction of the amount of lead slump. Figure 5.3 shows a detailed view of the end of the steel-lead-steel rail cask.

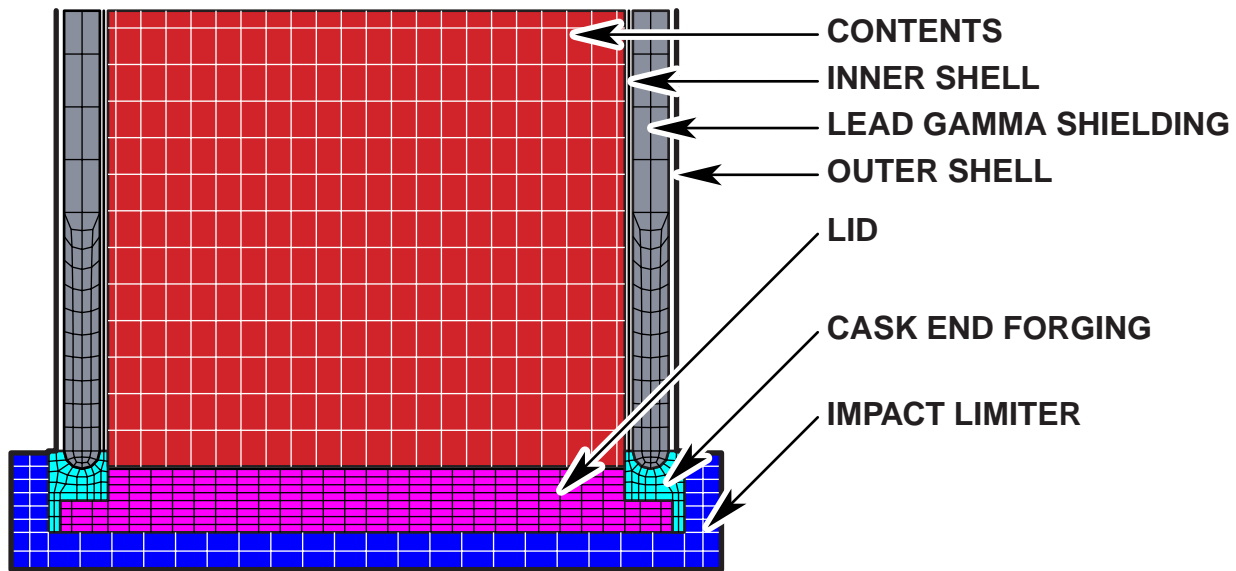


Figure 5.3 Detail of the end of the steel-lead-steel rail cask finite element model.

The behavior of the neutron shielding and its liner has little effect on deformations to the remainder of the cask, but any effect is beneficial. For this reason, these components are not modeled, but rather their mass is lumped with the mass of the contents to achieve the correct package weight. The contents and basket are treated as a homogenous crushable material. The crush strength of this material is chosen from the buckling strength of PWR fuel pins subjected to axial loads. The density of this material is adjusted so that the total weight of the cask is equal to the specified weight from Chapter 4. Modeling of the basket and contents in this manner does not allow direct determination of the behavior of the fuel rods, but provides an assessment of the loads that these components transmit into the structural portions of the cask. Because the only purpose of the contents within the model is to provide loading onto the cask, variations in their material properties has little effect on the analysis results. A description of how fuel behavior is determined from the finite element results is given in Section 5.4.

As indicated earlier, the crushing behavior of the impact limiters is not modeled. They are pre-crushed at the beginning of the analysis. To account for the post-crush behavior of the impact limiters they are treated as a solid with a density equivalent to a typical density for fully crushed aluminum honeycomb. The yield strength of this crushed material is typical for fully crushed 1000-psi aluminum honeycomb. The finite element model assumes that the entire impact limiter has been fully crushed, so the geometry in the model remains axi-symmetric. No attempt is made to model the attachments of the impact limiters; they are held in place only by inertia. If the inertial forces are not sufficient to keep the impact limiter in place during the impact event, then the cask body will impact directly onto the rigid surface. Real casks have impact limiter attachments that are usually designed so the impact limiters stay attached during the regulatory impact tests.

For all of the analyses, the initial velocity vector of the cask is assumed to be perpendicular to the rigid surface. All of the interior contact surfaces in the model (between the contents and the inner shell, the gamma shielding and both shells, the lid and the cask body, and the cask body and the impact limiter) are assumed to be frictionless. The contact between the cask and the rigid

surface is also frictionless. For most aspects of the problem this assumption is conservative, as there is no loss of impact energy because of frictional heating. Including friction at contact surfaces tends to cause the various parts of the modeled structure to behave more like a single piece (decreases separation of the parts of the structure being modeled). Including friction would also decrease the amount of impact energy available to cause structural deformation, as some of the energy would be absorbed by frictional heating. Lack of friction and the direction of the initial velocity guarantee that the displacement, velocity, and acceleration vectors will always be in a direction that is perpendicular to the rigid surface. This will be important when deriving the force-deflection curves for the casks in Section 5.2.2.

The closure of the cask is explicitly modeled. The lid is recessed into the body of the cask and held in place with either 12 (6 in the half-symmetric model) 1-inch diameter bolts for the truck casks or 24 (12 in the half-symmetric model) 1.75-inch diameter bolts for the rail casks. The bolt model cross-section is square with square heads. The area of the square bolt shank is the same as the area of a round bolt. The edges of the heads are rigidly attached to the cask lid, and the bottom of the shank is rigidly attached to the cask body. Figure 5.4 shows the cross-section through the center of a typical bolt and an isometric view of a single bolt. All of the contacts are tied via coincident nodes. The initial preload in the bolts caused by the torque applied to them when the cask is closed is neglected. Neglecting this preload is conservative because the preload must be overcome by loading from the contents before there is any deformation to the bolts. This factor makes a preloaded closure have smaller openings than a closure without preload.

Modeling the bolt in this way forces all of the deformation of the closure to take place in the short section that represents the shank of the bolt. Figure 5.5 shows how this method of modeling the bolt depicts shear deformations and tensile deformations. In a real closure, movement between the lid and the cask body will be accommodated by deformation of the bolt head and seat, sliding in the clearance hole, and stretching over a longer length of the bolt. These differences make the modeled bolts stiffer than the real bolts for tensile deformations, which leads to an over-prediction of bolt strain and an under-prediction of bolt stretch. Because the bolts (in the model and in reality) are much less stiff than the closure, the over-prediction of strain is much more significant than the under-prediction of displacement. The effect on leak area is discussed in section 5.1.4.

The O-ring grooves and O-rings for the seals are not included in the model, but the deformations in the sealing surfaces at the locations of the O-rings are tracked to determine when there is sufficient opening to cause permanent failure of the seal. From tests performed at Sandia on closure movements using 0.25-inch nominal O-rings, it has been determined that elastomeric O-rings can withstand greater than 0.070 inches of opening without losing their ability to contain helium at one atmosphere of differential pressure [5-6]. These O-rings had an initial pre-compression of about 0.075 inches. For the larger O-rings (compared to the Sandia study) typical of spent fuel casks, the larger amount of pre-compression implies there should be no material release for openings up to 0.100 inches.

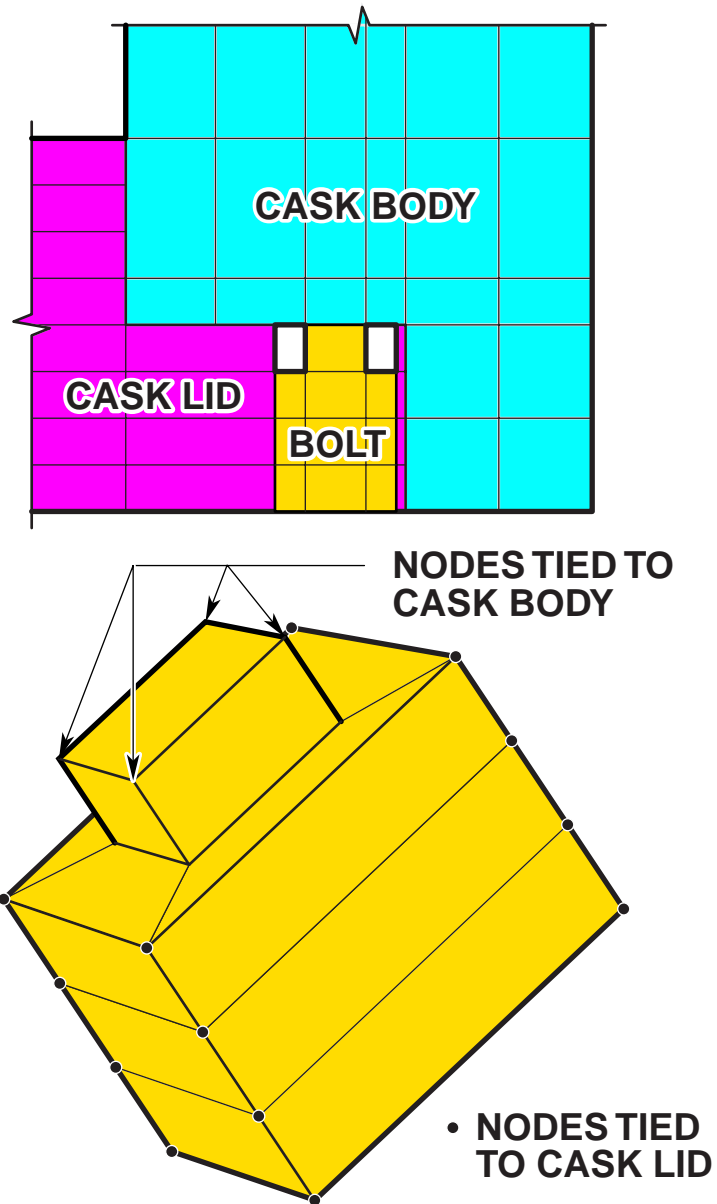


Figure 5.4 Typical model of a bolt used in the finite element analyses.

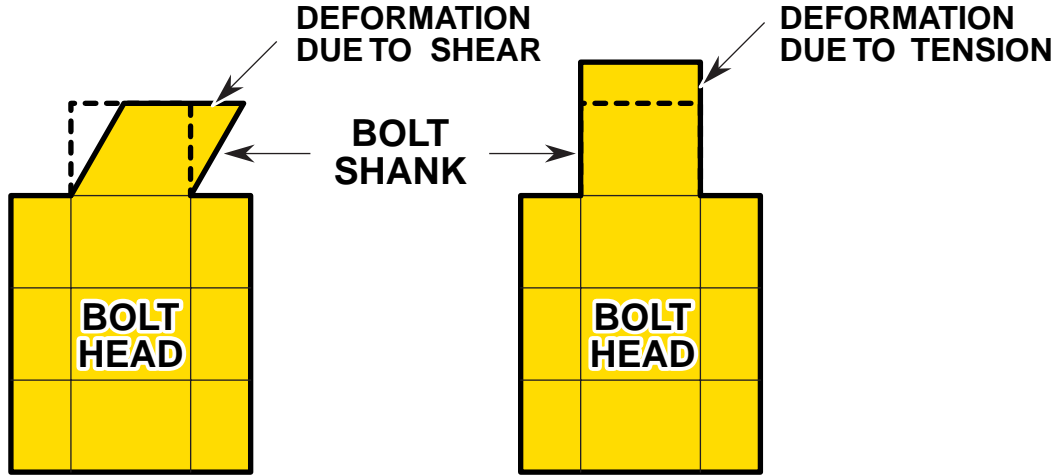


Figure 5.5 Modeling of the deformation in the bolts. The solid lines indicate the bolt position after being deformed and the dashed lines indicate the initial bolt position.

5.1.3 Material Models

The casks and contents modeled in this study consist of six different materials. The lids, ends, and structural portions of the walls are 304L stainless steel. The bolts are a high-strength stainless steel. The impact limiters are crushed aluminum honeycomb. The gamma shielding is either lead, depleted uranium, or stainless steel. The basket and spent fuel are modeled as a homogenized crushable material.

The stainless steel is modeled with a power-law hardening material model. This model treats the material as elastic up to the limit of proportionality and captures the plasticity by the equation:

$$\sigma = \sigma_p + A \langle \epsilon_p - \epsilon_L \rangle^n \quad (1)$$

where σ_p is the stress at the limit of proportionality, A is the hardening constant, ϵ_p is the equivalent plastic strain, ϵ_L is the Luder's strain (the flat portion of the stress-strain curve immediately after yielding for low-carbon steels), $\langle \rangle$ indicates the Heaviside function where the expression enclosed in the brackets is unchanged when positive and equal to zero when negative, and n is the hardening exponent.

For 304L stainless steel the parameters used are $\sigma_p = 28$ ksi, $A = 192.746$ ksi, $\epsilon_L = 0$, and $n = 0.74819$. For the elastic part of the curve $E = 28,000$ ksi and $\nu = 0.27$ [5-7].

The high-strength bolts (SA-540 Grade B23 Class 5 [5-8]) are modeled with a bi-linear elastic-plastic material model. The parameters used are $\sigma_y = 105$ ksi, $E = 30,000$ ksi, $\nu = 0.3$, and $E_p = 30$ ksi. The crushed aluminum honeycomb impact limiters are modeled using the power-law hardening model with $\sigma_p = 4250$ psi, $A = 32.7$ ksi, $\epsilon_L = 0$, $n = 0.325722$, $E = 9,900$ ksi and $\nu = 0.33$. The lead is modeled using the power-law hardening model with $\sigma_p = 2000$ psi,

$A = 800$ psi, $\epsilon_L = 0$, $n = 0.5$, $E = 2,000$ ksi and $\nu = 0.27$. These are the same material properties that were used in the benchmarking analyses of Ludwigsen and Ammerman [5-4]. The depleted uranium is modeled with a bi-linear elastic-plastic material model with $\sigma_y = 20$ ksi, $E = 28,000$ ksi, $\nu = 0.3$, and $E_p = 150$ ksi [5-9].

The homogenized basket and spent fuel are modeled with a material model originally developed for low-density polyurethane foams. This model is defined by the initial yield strength of the material (σ_y), initial elastic stiffness (E) and Poisson's ratio (ν), the hardening modulus (A), the solid material volume fraction (ϕ), the initial gas pressure in the material (p_o), and the strength of the solid portions (poly) [5-10]. For these analyses the values for the material properties are $\sigma_y = 1700$ psi, $A = 1700$ psi, $\text{poly} = 30,000$ psi, $p_o = 14.7$ psi, $\phi = 0.6$, $E = 1000$ ksi, and $\nu = 0.0$.

A summary of the material properties for all of the materials used in the analyses is given in Table 5.2. All of these material models accurately capture the three-dimensional state of stress and strain within finite element analyses.

Table 5.2 Material Properties Used in the Finite Element Analyses

Item	Material Model	E (ksi)	ν	σ_y or σ_p (ksi)	A or E_p (ksi)	n	poly (ksi)	ϕ	p_o (psi)
Stainless Steel	Power-law hardening	28,000	0.27	28	193	0.7482			
Bolts	Elastic-plastic	30,000	0.30	105	30				
Impact Limiters	Power-law hardening	9,900	0.33	4.25	32.7	0.3257			
Lead	Power-law hardening	2,000	0.27	2	0.8	0.5			
Depleted Uranium	Elastic-plastic	28,000	0.3	20	150				
Contents	Crushable	1,000	0.0	1.7	1.7		30	0.6	14.7

5.1.4 Finite Element Results

Using finite element analyses to determine the ability of the casks to maintain containment requires investigation of all of the areas and factors that may result in a loss of containment. For these casks the main factors to consider are maximum tensile plastic strains in the containment boundary, maximum tensile plastic strains in the closure bolts, and deformations in the region of the seals. For the sandwich-wall casks the containment boundary is the inner shell, but the development of a tear in this shell does not necessarily imply a loss of containment if the outer shell remains intact. None of the finite element impact analyses indicated strains above 70 percent in this shell, so no tearing is predicted to take place (the true strain at failure for 304L is

greater than 120 percent). Table 5.3 shows the maximum level of plastic strain observed in the inner shell for the three sandwich wall casks. The strain levels in the other portions of the cask were lower than those in the shells. A strain fringe plot for the 120-mph impact of the steel-lead-steel truck cask is shown in Figure 5.6. EQPS is the equivalent plastic strain, and is the non-directional three-dimensional measure of stretching in the material. Similar figures for all of the analyses are given in Appendix A.

Table 5.3 Maximum Plastic Strain in the Inner Shell of the Sandwich Wall Casks

Cask	Corner Impact		End Impact		Side Impact	
	Speed	Strain (%)	Speed	Strain (%)	Speed	Strain (%)
Steel-Lead-Steel Truck	30 mph	12	30 mph	3.9	30 mph	n.a.
	60 mph	29	60 mph	12	60 mph	16
	90 mph	33	90 mph	18	90 mph	24
	120 mph	47	120 mph	27	120 mph	27
Steel-DU-Steel Truck	30 mph	11	30 mph	1.8	30 mph	6
	60 mph	27	60 mph	4.8	60 mph	13
	90 mph	43	90 mph	8.3	90 mph	21
	120 mph	55	120 mph	13	120 mph	30
Steel-Lead-Steel Rail	30 mph	21	30 mph	1.9	30 mph	5.9
	60 mph	34	60 mph	5.5	60 mph	11
	90 mph	58	90 mph	13	90 mph	15
	120 mph	70	120 mph	28	120 mph	n.a.

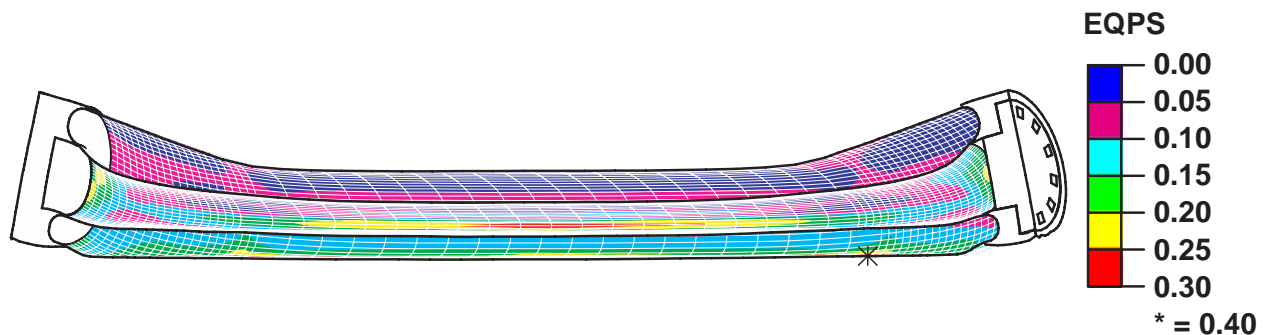


Figure 5.6 Deformed shape and plastic strain fringes for the steel-lead-steel truck cask following a 120-mph impact in the side-on orientation. The maximum plastic strain (indicated by the asterisk) occurs in the outer shell. The maximum strain in the inner shell is 0.27.

For the monolithic rail cask the maximum strain on the interior surface of the cask is less than 60 percent for all analyses. The maximum occurs at the lid-cask interface for the 120-mph side impact case. At this location most of the plasticity is caused by compression, so there is no possibility of material failure. Table 5.4 lists the maximum strains on the inside of the cask for these analyses.

Table 5.4 Maximum Plastic Strains on the Inside of the Monolithic Rail Cask

Corner Impact		End Impact		Side Impact	
Speed	Strain (%)	Speed	Strain (%)	Speed	Strain (%)
30 mph	< 10	30 mph	< 2	30 mph	< 10
60 mph	< 20	60 mph	< 5	60 mph	< 30
90 mph	< 30	90 mph	< 10	90 mph	< 50
120 mph	< 50	120 mph	< 17	120 mph	< 60

The chance of a closure failure is directly related to the deformations between the cask lid and cask body and tensile or shear failure of the bolts. For the conservative bolt model used in these analyses, the maximum strain in any of the bolts is shown in Table 5.5. Several of these analyses indicate bolt strains that are high enough that failure of the bolt is likely (strains greater than 50 percent). The bolt material has a specified percent elongation greater than 15 percent and a specified percent reduction of area greater than 50 percent [5-8]. This correlates to a true strain at failure of 69 percent. A value of 50 percent is conservatively chosen to indicate bolt failure because the material model used for the bolts has the true stress in the bolts equal to the ultimate tensile stress (an engineering stress) at a strain of 50 percent. Limiting the bolt stress to the ultimate tensile stress also assures that the bolt threads will not fail. Bolt true strains that are higher than 50 percent are shown in **bold** in the table. Several other analyses indicate bolt strains that are high enough that failure of the bolts is possible (true strains higher than 25 percent). These bolt strains are shown in *italics* in the table. Analysis for one of the cases where bolt strains indicate that bolt failure could occur including a failure model for bolts with strains greater than 50 percent shows that even if some of the bolts fail, the remaining bolts will hold the lid in place. Comparison of the closure deformations for this case with those for the same case without the bolt failure model indicates only minor differences (less than 20% for the side impact and only a few percent for the corner impact). This is because the bolt loads are primarily caused by a displacement discontinuity between the cask body and the lid.

Table 5.5 Maximum True Strain in the Closure Bolts

Cask	Corner Impact		End Impact		Side Impact	
	Speed	Strain (%)	Speed	Strain (%)	Speed	Strain (%)
Steel-Lead-Steel Truck	30 mph	3	30 mph	1	30 mph	n.a
	60 mph	6	60 mph	3	60 mph	2
	90 mph	9	90 mph	5	90 mph	5
	120 mph	11	120 mph	7	120 mph	10
Steel-DU-Steel Truck	30 mph	5	30 mph	0	30 mph	1
	60 mph	9	60 mph	3	60 mph	4
	90 mph	19	90 mph	7	90 mph	10
	120 mph	22	120 mph	9	120 mph	18
Steel-Lead-Steel Rail	30 mph	19	30 mph	6	30 mph	14
	60 mph	37	60 mph	3	60 mph	106
	90 mph	60	90 mph	9	90 mph	151
	120 mph	102	120 mph	16	120 mph	n.a.
Monolithic Rail	30 mph	14	30 mph	4	30 mph	15
	60 mph	40	60 mph	14	60 mph	32
	90 mph	67	90 mph	35	90 mph	104
	120 mph	80	120 mph	58	120 mph	170

The amount of deformation between the cask body and the lid at the location of the O-ring seals determines if a leak path from the cask is generated. Because the seal grooves were not explicitly included in the model, the deformation at a location that is near where the O-rings would be located is used. For each model the displacement of two sets (upper point and lower point) of two nodes on the cask lid and one node on the cask body are tracked for all times. Initially these three nodes are co-linear, with the body node lying between the two lid nodes. From the displacement time histories, the amount of seal separation and seal sliding can be determined. The seal separation is defined as the movement of the body node that is normal to the line between the two lid nodes. The sliding is defined as the movement of the body node along the line between the two lid nodes. Figure 5.7 shows these displacements for the 90-mph end impact of the monolithic steel rail cask. Figure 5.8 shows a typical time history for opening displacement. Similar curves for all of the analyses are included in Appendix A. Table 5.6 shows the seal region displacements at the end of the finite element analysis. Because the only location for leakage of radioactive materials is at the closure, and the high degree of variability in closure designs, identical analyses with less stiff bolts were performed for the 60 mph corner and side impacts of the monolithic steel rail cask. To perform these analyses the elastic modulus and strain-hardening modulus of the bolt steel were reduced by a factor of three. These analyses resulted in nearly identical opening displacements as the original analyses. These results support the hypothesis that the cask wall and lid are much stiffer than the closure bolts, and the opening displacements are the result of displacement discontinuities between the cask body and lid, and are not greatly affected by bolt clamping force.

For the end-on impact orientation analyses the displacements at the end of the finite element run had not reached a stable value. For these analyses a range of final displacements is given in the table. This oscillatory response is caused by the lack of friction and material damping within the finite element model. Numerically these oscillations will continue while the cask is rebounding. In reality, the friction and other damping mechanisms will quickly cause these oscillations to stop, and the final displacements will be at about the middle of the range shown in the table.

The many factors affecting closure opening and the way they interact can lead to surprising results. For example, the maximum true strain in the closure bolts for the lead shielded rail cask is higher for the 30-mph impact than it is for the 60-mph impact. In addition, for many of the impacts increasing the impact velocity results in a decrease in closure opening as shown in Table 5.6.

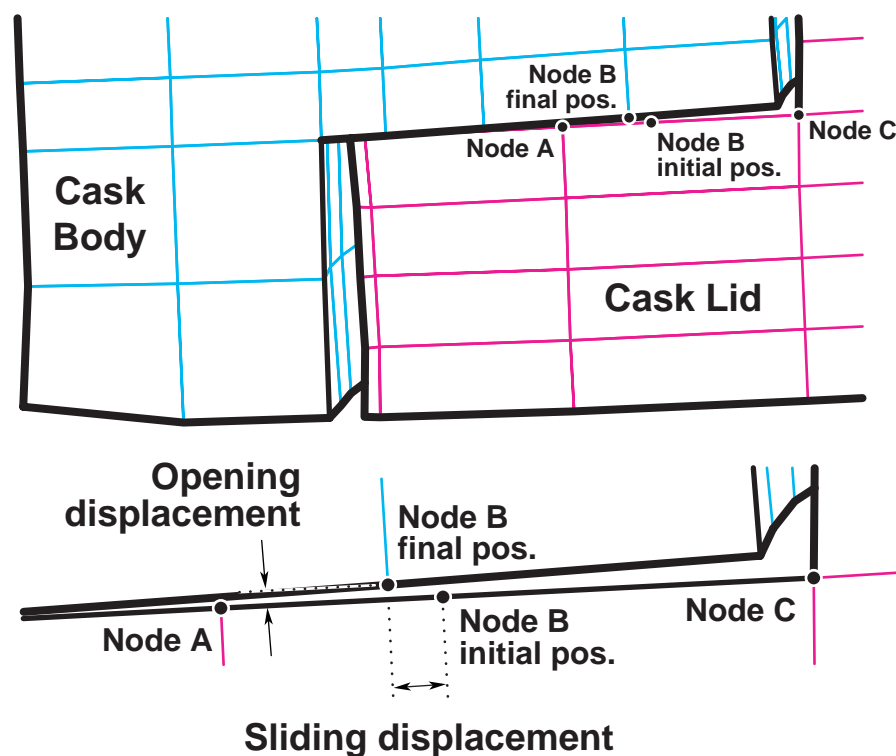


Figure 5.7 Seal region displacements for the 90-mph end impact of the monolithic steel rail cask.

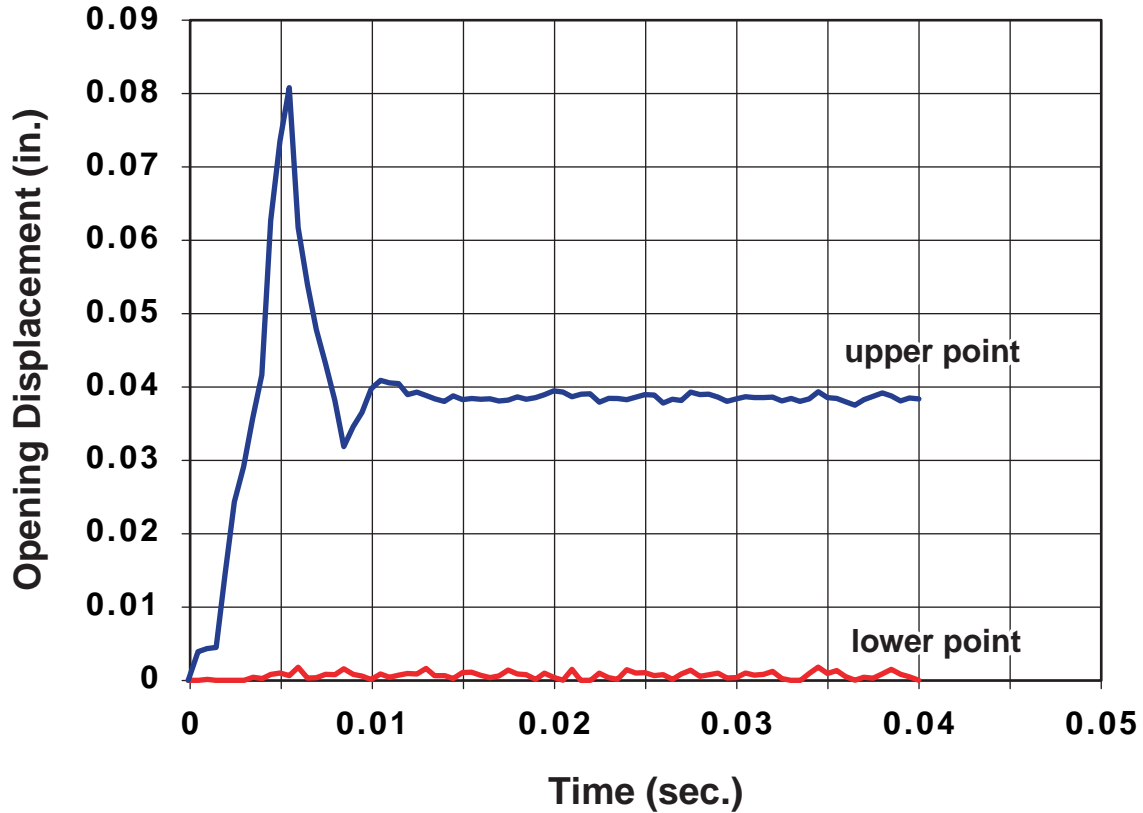


Figure 5.8 Time history for lid opening displacement for the 60 mph side-impact of the monolithic steel rail cask.

Table 5.6 Seal Closure Displacements, in Inches, at the End of the Analysis

Cask	Analysis Velocity	Corner Impact		End Impact		Side Impact	
		Opening	Sliding	Opening	Sliding	Opening	Sliding
Steel-Lead-Steel Truck	30 mph	0.02	0.01	0.000-0.002	0.000-0.002	-	-
	60 mph	0.02	0.03	0.001-0.003	0.001-0.004	0.01	0.02
	90 mph	0.02	0.06	0.000-0.002	0.003-0.005	0.02	0.02
	120 mph	0.04	0.04	0.002	0.02	0.02	0.01
Steel-DU-Steel Truck	30 mph	0.02	0.07	0.005-0.012	0.001-0.005	0.01	0.02
	60 mph	0.08	0.07	0.01-0.02	0.003-0.006	0.01	0.01
	90 mph	0.02	0.10	-	-	0.01	0.02
	120 mph	0.03	0.15	0.013	0.03	0.004	0.02
Steel-Lead-Steel Rail	30 mph	0.01	0.14	0.001-0.022	0.009-0.012	0.01	0.02
	60 mph	0.08	0.32	0.000-0.016	0.01-0.02	0.02	0.01
	90 mph	0.24	0.74	0.004-0.005	0.097-0.101	0.02	0.02
	120 mph	0.51	1.18	0.001-0.018	0.20-0.22	-	-
Monolithic Rail	30 mph	0.04	0.20	0.007-0.053	0.04-0.05	0.01	0.01
	60 mph	0.10	0.36	0.04-0.12	0.09-0.10	0.04	0.01
	90 mph	0.22	0.48	0.03-0.13	0.38-0.39	0.08	0.09
	120 mph	0.44	0.59	0.09-0.16	0.668	0.12	-

To determine the leak area that results from these opening displacements, the influence of the pre-compression of the elastomeric O-ring and the width of the opening must be considered. For cases with maximum openings of less than 0.100 inches, the pre-compression of the O-ring (as much as 0.112 inches for 3/8-inch O-rings and 0.150 inches for 1/2-inch O-rings at 30 percent compression for static face seal configurations [5-11]) will allow it to recover sufficiently to maintain an adequate seal to prevent release of radioactive material. For opening displacements between 0.100 and 0.200 inches, the difference in bolt strains indicates that the opening only occurs at the location of one bolt. The width of the leak path is then equal to the bolt spacing (6.38 inches for the rail casks). However, for part of this width, the actual opening displacement will be less than the O-ring compression; therefore, the area of the resulting hole is calculated by truncating the base (the truncated part has a height of 0.100 inches) of an isosceles triangle with a height of the opening displacement and a width of the bolt spacing. For opening displacements between 0.200 and 0.300 inches, the opening occurs over two bolt spacings, and for opening displacements greater than 0.300 inches, it is assumed the opening occurs over three bolt spacings. For opening displacements greater than 0.300 inches, the resulting leak area is sufficiently large that increasing the width of the opening has little or no effect on the amount of release. Table 5.7 summarizes the leak path calculations for the analyses where the maximum closure opening is greater than 0.100 inches.

Table 5.7 Calculated Rail Cask Closure Hole Sizes

Cask	Velocity (mph)	Orientation	Opening Displacement (inches)	Opening Width (inches)	Leak Path Area (in ²)
Steel-Lead-Steel Rail	90	Corner	0.243	12.76	0.54
	120	Corner	0.512	19.14	3.2
Monolithic Rail	60	Corner	0.103	6.38	0.00028
	90	Corner	0.216	12.76	0.40
	120	Corner	0.439	19.14	2.5
	120	Side	0.123	6.38	0.014

An additional result of impact accidents can be loss of shielding. For the two lead-shielded casks, loss of shielding is a result of the slumping of the lead. For the monolithic steel rail cask there is no loss of shielding, but there may be some radiation streaming through the closure. For the steel-DU-steel truck cask, the model does not include any gaps between forged DU segments, so there is no loss of shielding. Lead slump occurs mostly in the end-on impact orientation, with a lesser amount in the CG-over-corner orientation. In the side-on orientation there is no significant reduction in shielding. The zero-thickness shell elements in the finite element model allow the lead additional space to flow to before contacting the wall. This increases the observed amount of lead slump. Figure 5.9 shows the steel-lead-steel rail cask following a 120-mph end impact.

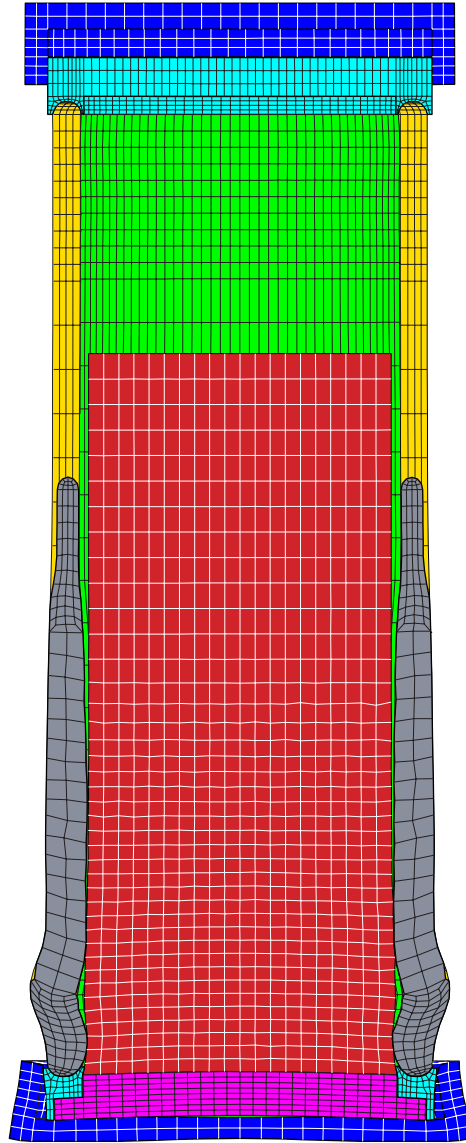


Figure 5.9 Slumping of lead and contents following a 120-mph end-on impact of the steel-lead-steel rail cask.

5.1.5 Benchmarking of Finite Element Calculations

Typical analyses used to certify a cask do not indicate the large levels of strains seen in these analyses. To be confident that analyses of this type are capturing the true response of the package they must be compared to similar analyses that have been demonstrated to be accurate. In the mid 1990s Sandia performed a series of tests and analyses of the Structural Evaluation Test Unit (SETU). End impact tests of 30, 45, and 60 mph were performed. This test unit was roughly a 1/3-scale model of a steel-lead-steel walled rail cask. In this program excellent agreement was obtained between two-dimensional axi-symmetric finite element analyses and end impact tests. In addition, a 7 degrees off-axis impact test at 60 mph was performed and compared to 3-D finite element calculations. Again there was excellent agreement between the analysis and test results. The finite element models used in the SETU program were very similar

to those used here [5-4]. For the 3-D finite element analysis the inner and outer shells were modeled using the same shell elements as this report. However, in the SETU analyses the location of the zero-thickness shell elements was adjacent to the lead because there was no possibility for 2-sided contact on the shells. Appendix B of this report gives a detailed description of the SETU analyses.

5.2 Impacts onto Real Targets

5.2.1 Introduction

The finite element results discussed in the previous section are all for impacts onto a rigid target. For this type of impact, the entire kinetic energy of the impact is absorbed by the cask. For finite element analyses a rigid target is easily implemented by enforcing a no displacement boundary condition at the target surface. In real life, the construction of a rigid target is impossible, but it is possible to construct a target that is sufficiently rigid that increasing its rigidity does not increase the amount of damage to the cask. This is because in real impacts there is a sharing of energy absorption between the cask and the target. If the target is much weaker than the cask, the target will absorb most of the energy. If the target is much stronger than the cask, most of the energy will be absorbed by the cask. In this section the partitioning of the drop energy between the four generic casks and several “real-world” targets will be developed in order to obtain impact speeds onto real surfaces that give the same damage as impacts onto rigid targets. Impacts onto hard desert soil, concrete highways, and hard rock are considered. Impacts onto water surfaces are not explicitly treated, but are discussed. In addition, the probability of puncture of the cask caused by impact against a non-flat surface (or impact by a puncture probe) is developed.

5.2.2 Methodology

The finite element analyses discussed in the preceding sections were all conducted assuming the impact limiter had already been fully crushed. As a result, it is not possible to use these analyses to determine real target impact velocities that equate to the regulatory impact. Impact limiters are typically designed to protect the baskets and spent fuel in a cask from high accelerations. For this reason, most spent-fuel casks have very similar impact limiter designs. Cask behavior for regulatory impacts is primarily a function of impact limiter design, and not cask design. This allows the results from the Modal Study [5-15] steel-lead-steel casks (which included the impact limiters for 30-mph impacts) to be used for the generic casks used in this study to determine equivalent real target impact velocities at rigid target impact velocities of 30 mph. Therefore, for impacts onto real targets that equate to the regulatory impact, the results from the Modal Study are used for all surfaces except hard rock. For the hard rock impacts it is assumed the target absorbs no energy and the equivalent velocity is equal to the rigid target velocity. For impacts at higher velocities, the methodology described below is used.

For each finite element calculation for impact onto a rigid target the total kinetic energy of the finite element model is output at 100 time-steps through the analysis. The total kinetic energy is one half of the sum of the mass associated with each node times the velocity of that node squared. Figure 5.10 shows kinetic energy time-histories for the steel-lead-steel truck cask for

each orientation from the 120-mph impact analyses with pre-crushed impact limiters. From the time-history of kinetic energy, a velocity time history is derived. The rigid-body velocity for each time-step is calculated assuming that all of the kinetic energy of the model is caused by velocity in the direction of the impact. Equation 2 shows this mathematically.

$$V_t = \sqrt{\frac{2KE_t}{\sum m_i}} \quad (2)$$

where v_t is the velocity at time t , KE_t is the kinetic energy at time t , m_i is the mass associated with node i , and the summation is over all of the nodes in the finite element model.

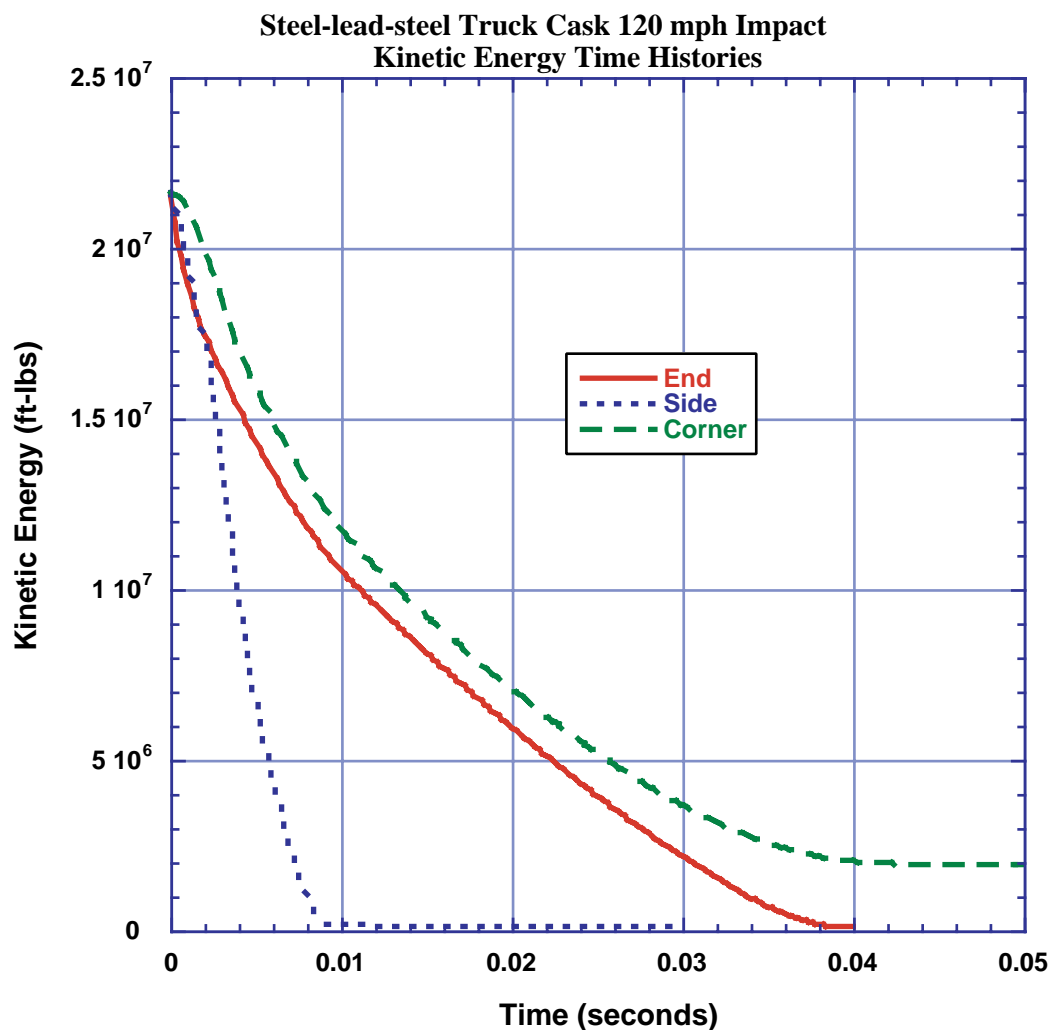


Figure 5.10 Kinetic energy time histories for the steel-lead-steel truck cask from 120-mph impact analyses in the end, side, and corner orientations.

Numerical integration of the velocity time-history gives the displacement of the center-of-gravity of the model. A large portion of this displacement is the result of the center-of-gravity moving down from the geometric center of the cask due to lead and contents slump. Numerical differentiation of the velocity time-history gives rigid-body acceleration. The contact force between the rigid target and the cask at any time is assumed to be equal to the rigid-body acceleration times the mass of the cask. This results in a force time-history. Combination of the force time-history and the displacement time-history results in a force-deflection curve for each cask and impact velocity. Figure 5.11 shows the force deflection curves derived from the kinetic energy time-histories shown in Figure 5.10. Numerical integration of the force-deflection curve results in energy absorbed by the cask. At the end of the analysis the energy absorbed by the cask is equal to the initial kinetic energy.

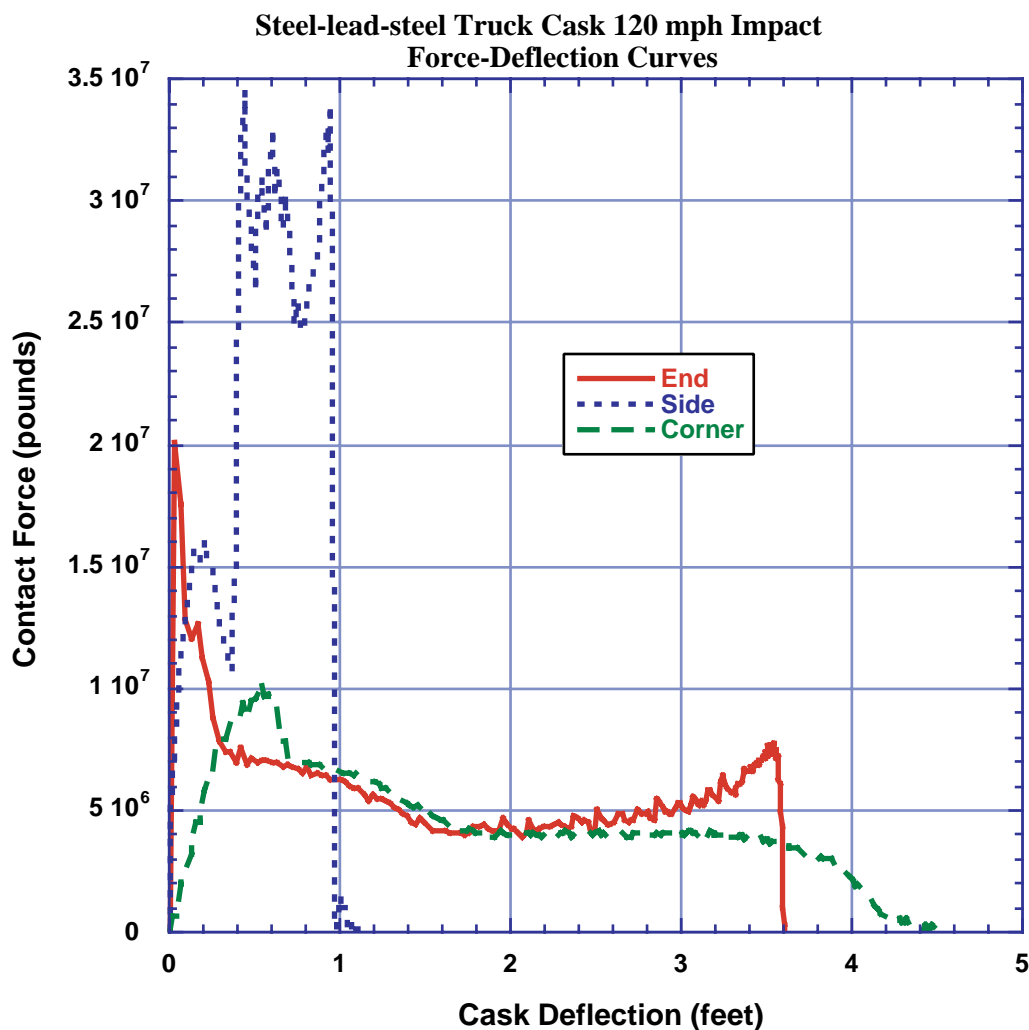


Figure 5.11 Force-deflection curves for the steel-lead-steel truck cask from the 120-mph impact analyses in the end, side, and corner orientations.

For each analysis the peak contact force is determined. Table 5.8 lists these forces. For an impact onto a real target to be as damaging to the cask as the impact onto the rigid target, the target must be able to impart a force equal to this peak force to the cask.

The energy absorbed by the target in developing this force is added to the initial kinetic energy of the cask. This total absorbed energy is used to calculate an equivalent velocity by replacing KE_i in Equation 2 with the total energy.

Table 5.8 Peak Contact Force From Impacts Onto Rigid Targets (Pounds)

Cask	Corner Impact		End Impact		Side Impact	
Steel-Lead-Steel Truck	30 mph	2.3E6	30 mph	9.0E6	30 mph	5.7E6
	60 mph	5.0E6	60 mph	1.3E7	60 mph	1.4E7
	90 mph	7.0E6	90 mph	1.7E7	90 mph	2.2E7
	120 mph	1.0E7	120 mph	2.0E7	120 mph	3.4E7
Steel-DU-Steel Truck	30 mph	6.5E6	30 mph	1.0E7	30 mph	9.0E6
	60 mph	1.1E7	60 mph	1.3E7	60 mph	2.3E7
	90 mph	1.4E7	90 mph	1.5E7	90 mph	3.4E7
	120 mph	1.7E7	120 mph	1.7E7	120 mph	4.9E7
Steel-Lead-Steel Rail	30 mph	1.3E7	30 mph	3.8E7	30 mph	1.8E7
	60 mph	2.3E7	60 mph	6.8E7	60 mph	4.4E7
	90 mph	3.6E7	90 mph	8.3E7	90 mph	6.2E7
	120 mph	n.a.	120 mph	1.1E8	120 mph	n.a.
Monolithic Rail	30 mph	2.1E7	30 mph	3.8E7	30 mph	2.2E7
	60 mph	3.9E7	60 mph	9.5E7	60 mph	5.4E7
	90 mph	5.8E7	90 mph	1.1E8	90 mph	9.5E7
	120 mph	7.5E7	120 mph	1.3E8	120 mph	1.1E8

5.2.3 Soil Targets

The force that hard desert soil imparts onto a cask following an impact was derived from results of impact tests performed by Gonzales [5-13], Waddoups [5-14], and Bonzon and Schamaun [5-15]. The tests by Gonzales and Waddoups used casks that were comparable to the generic casks of this study. The tests by Bonzon and Schamaun were with casks that were less stiff than the generic casks. This large amount of test data was used to develop an empirical soil target force-deflection equation that is a function of impactor area. Figure 5.12 shows the force-deflection curves for impact of the steel-lead-steel truck cask. Corner impacts were assumed to have the same contact area on the soil target as the end impacts, so only two curves are shown. Similar curves were developed for each of the other casks. Comparison of Figure 5.12 with the forces in Table 5.8 show that many of the impacts will result in very large soil penetrations. This is consistent with the results seen in Waddoups' tests, where casks were dropped 2,000 feet from a helicopter. Penetration depths for these impacts were up to 8 feet, and the equivalent rigid target impact velocity was less than 30 mph. Integration of the force-deflection curve up to the peak contact force determines the amount of energy absorbed by the target.

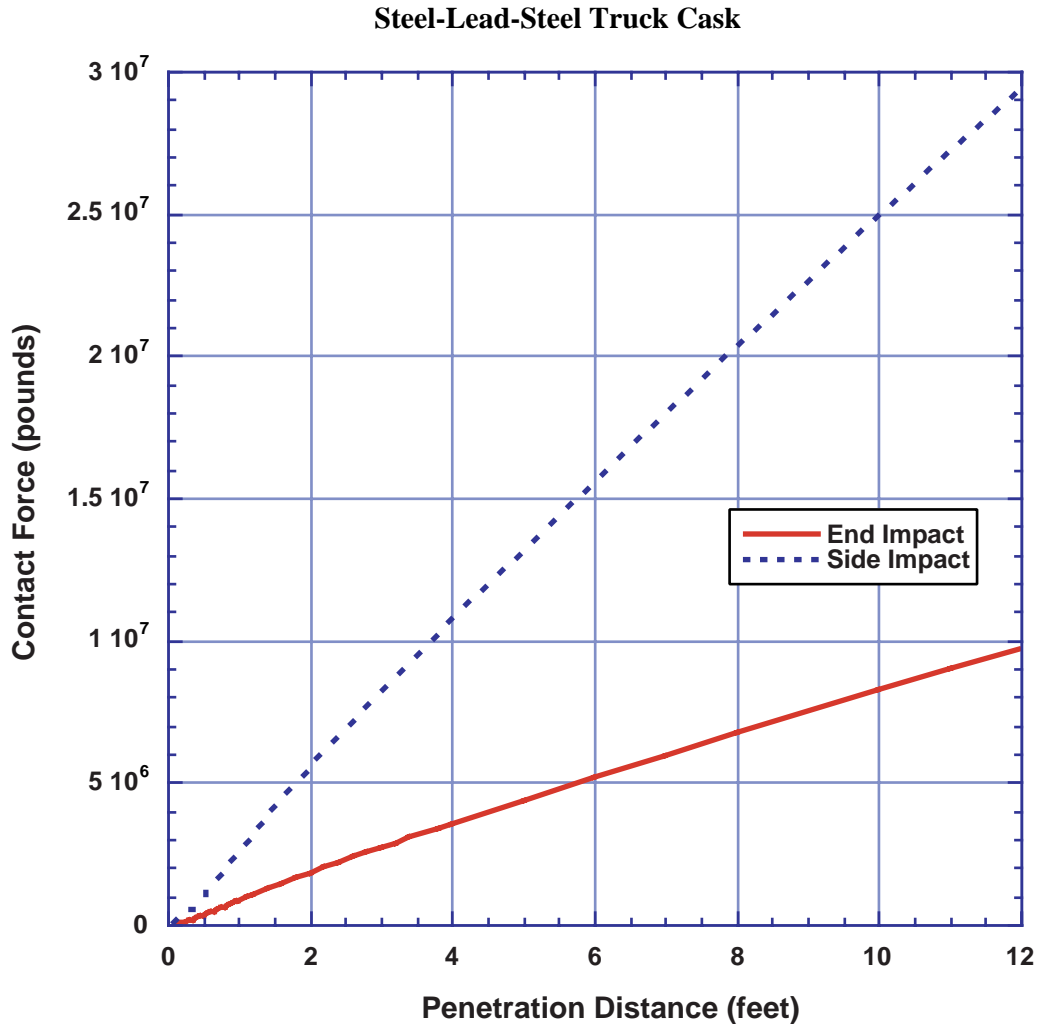


Figure 5.12 Force-deflection curves for impact onto hard desert soil.

5.2.4 Concrete Targets

The force imparted to a cask by impact onto a concrete target is derived from test results by Gonzales [5-13]. In his series of tests, a cask-like test unit was impacted onto two types of concrete targets, one 12 inches thick and one 18 inches thick, at velocities from 30 to 60 mph. All of the impacts were in an end-on orientation. Based upon the results of these tests and engineering mechanics, an empirical relationship between the force and energy absorbed was derived. For impacts onto concrete slab targets there are two mechanisms that produce large forces onto the cask. The first is the generation of a shear plug in the concrete. The force required to produce this shear plug is linearly related to the impact velocity, the diameter of the impacting body, and the thickness of the concrete. Equation 3 gives the empirical equation for the force required to produce the shear plug.

$$F_s = C_s v_e d_i t_c \quad (3)$$

where F_s is the force required to produce the shear plug, C_s is an empirical constant (16.84), v_e is the equivalent impact velocity, d_i is the diameter of the impactor, and t_c is the thickness of the concrete slab.

The energy absorbed in producing this shear plug is linearly related to the cask diameter, the square of the impact velocity, and the fourth root of the slab thickness. Equation 4 gives the empirical equation for the energy required to produce the shear plug.

$$E_s = C_e d_i v_e^2 t_c^{0.25} \quad (4)$$

where E_s is the energy required to produce the shear plug and C_e is an empirical constant (0.00676).

After the shear plug is formed, further resistance to penetration is achieved by the behavior of the subgrade and soil beneath the concrete. This material is being penetrated by the cask and the shear plug. Generally, the shear plug forms with 45-degree slopes on the side. Therefore, the diameter of the soil being penetrated is equal to the cask diameter plus twice the slab thickness. The behavior of the subgrade and soil is assumed to be the same as the hard desert soil used for the soil target impacts. Figure 5.13 shows a comparison of the empirical relationship with one of Gonzales' tests. Figure 5.14 shows the force-deflection curve for the steel-lead-steel truck cask impacting a 9-inch thick concrete roadway at 120 mph. For corner and side impacts an equivalent diameter is calculated to fit with the empirical equations. For each case the diameter is calculated by assuming the shear plug forms when the concrete target has been penetrated two inches. The area of the equivalent diameter is equal to the area of the concrete in contact with the cask when the penetration depth is two inches. To calculate the equivalent velocity for concrete targets the force required to generate the shear plug must be compared to the peak contact force for the impact onto the rigid target. The velocity required to produce this force can be calculated from Equation 3. The kinetic energy associated with this velocity is absorbed by a combination of producing the shear plug, penetration of the subgrade and soil beneath the concrete, and deformation of the cask. The energy absorbed in producing the shear plug is calculated by Equation 4, the energy absorbed by the cask is equal to the kinetic energy of the rigid target impact, and the energy absorbed by the subgrade and soil is calculated in a manner similar to that for the soil impact discussed above. If the amount of energy to be absorbed by the soil is sufficiently high, the force in the soil will be higher than the force required to produce the shear plug. In this case, an iterative approach is necessary to derive an equivalent velocity so that the maximum force generated in penetrating the subgrade and soil beneath the concrete is equal to the peak contact force for the rigid target impact.

Gonzales Impacts onto Highway Targets

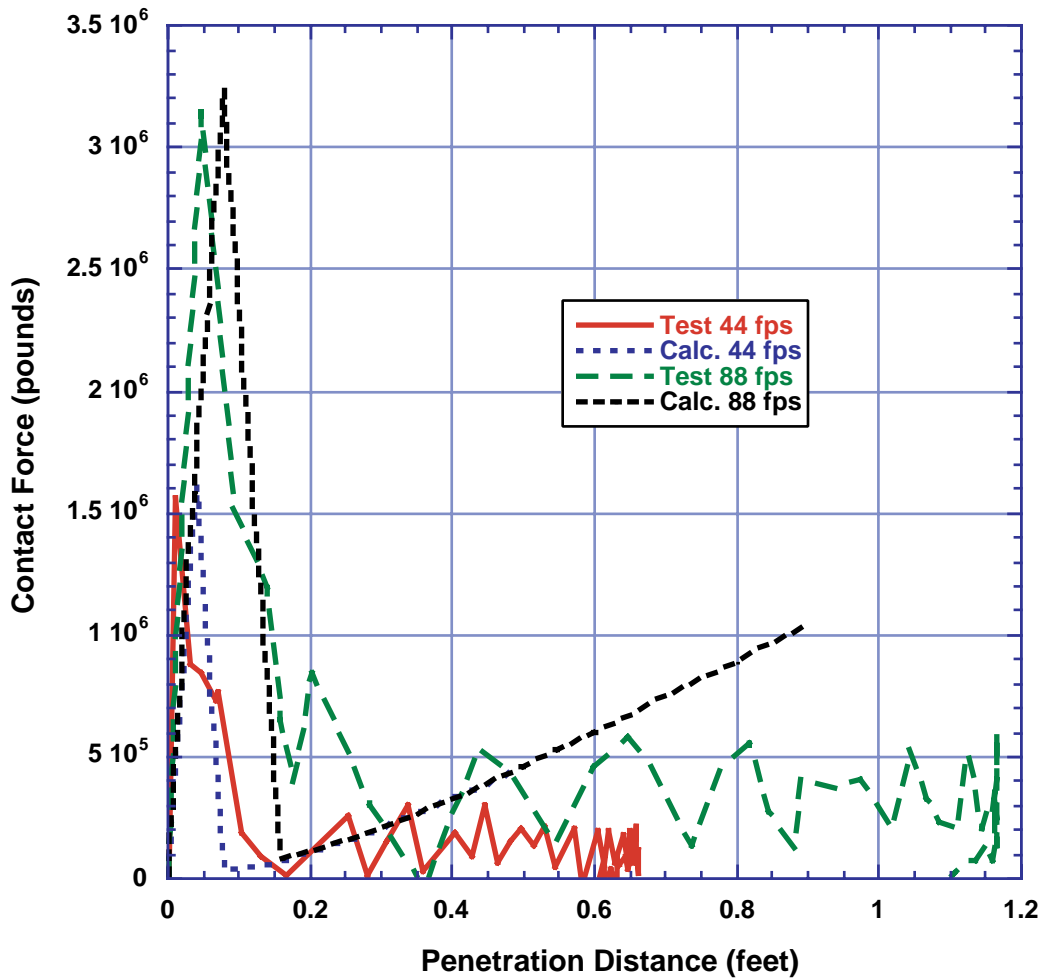


Figure 5.13 Comparison of test force-deflection curves with those derived from the empirical equations.

The only orientation of impacts onto concrete targets where test data is available is for end impacts. In this orientation the contact area between the cask and the concrete does not increase with increasing penetration distance. In order to use the empirical relationships developed for end impacts with other impact orientations, an equivalent diameter must be determined. For both the side and corner impacts, the equivalent diameter was calculated to have an area equal to the area of the cask two inches above the contact point. For side impact orientations, this area is a rectangle. For corner impact orientations this area is a truncated parabola. Table 5.9 gives the equivalent diameters used for each of the casks. For all of the casks, the equivalent diameter for the corner impact is much smaller than the cask diameter. This is especially pronounced for the rail casks. In reality, the failure mode for a concrete target being impacted by a large cask in a corner orientation is probably not generation of a shear plug, but rather a splitting tensile failure and subsequent rotation of the slab to allow perforation by the cask. After penetration of the concrete occurs, the area of the cask plus concrete penetrating the soil is equal to the cask cross-sectional area (the same area used for the soil target impacts).

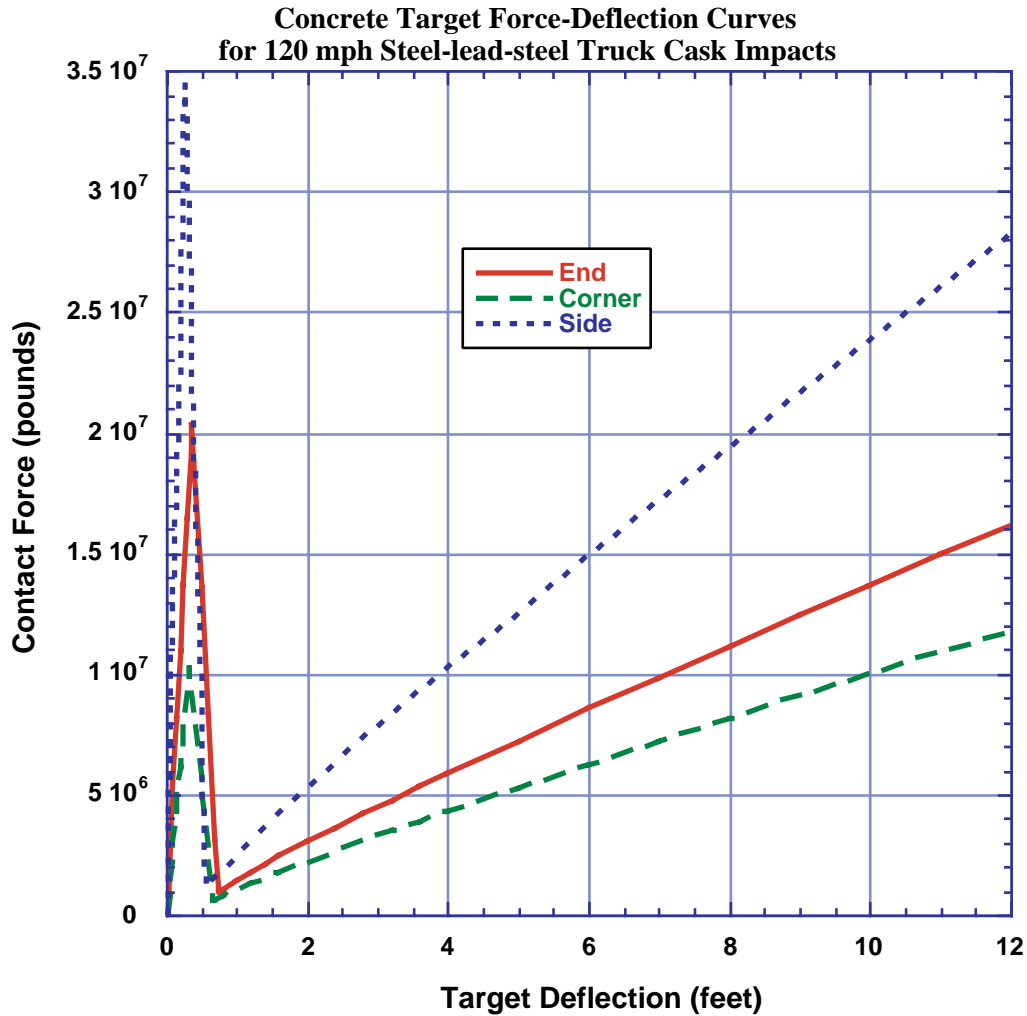


Figure 5.14 Force-deflection curves for concrete target impacts of the steel-lead-steel truck cask at 120 mph.

Table 5.9 Equivalent Diameters for Concrete Impacts

Cask	Orientation	Equivalent Diameter (inches)
Steel-Lead-Steel Truck	Corner	15.3
	End	27.5
	Side	61.1
Steel-DU-Steel Truck	Corner	20.2
	End	28.0
	Side	60.6
Steel-Lead-Steel Rail	Corner	13.6
	End	80.0
	Side	79.8
Monolithic Rail	Corner	13.0
	End	85.0
	Side	79.0

5.2.5 Hard Rock Targets

For impacts onto hard rock targets the target is assumed to be a semi-infinite half plane. The force and energy absorbed by the target is determined by the volumetric behavior of the rock. For hard rock surfaces this behavior is sufficiently stiff that very little energy is absorbed by the target. For this reason these impacts are treated as rigid target impacts.

5.2.6 Example Calculation

In this section, the methodology discussed in Section 5.2.2 will be applied to the steel-lead-steel truck cask using the soil target properties from Section 5.2.3. For the 120 mph impact in the end-on orientation the peak contact force acting on the cask is 20×10^6 pounds (from Figure 5-11 or Table 5-8). For a soil target to generate this amount of force, the cask must penetrate slightly over 12 feet (from Figure 5.12). The energy absorbed by the soil target while it is being penetrated to this distance is equal to the integral under the force-deflection curve up to this penetration distance. For this case, this is equal to 136×10^6 foot-pounds. The kinetic energy of this 50,000 pound cask travelling at 120 mph is 24.1×10^6 foot-pounds. This is the amount of energy absorbed by the cask for impact onto a rigid target. For the impact onto the soil target, the cask will therefore absorb 24.1×10^6 foot-pounds of energy and the soil will absorb 136×10^6 foot-pounds of energy for a total of 160×10^6 foot-pounds of energy. The cask velocity that is associated with this amount of kinetic energy is 309 mph. This velocity is much higher than the 150-mph top velocity in the accident velocity distributions. Note that all of the equivalent velocities determined in this manner neglect the energy absorbed by the impact limiter.

5.2.7 Results for Real Target Calculations

Tables 5.10 to 5.13 summarize the results for impacts onto soil and concrete targets.

Table 5.10 Real target Equivalent Velocities (mph) for the Steel-Lead-Steel Truck Cask

Target/Orientation	Rigid Target Velocity			
	30 mph w/o limiter	60 mph w/o limiter	90 mph w/o limiter	120 mph w/o limiter
Soil				
End	>150	>>150	>>150	>>150
Side	70	>150	>>150	>>150
Corner	61	135	>150	>>150
Concrete Slab				
End	123	>150	>>150	>>150
Side	35	86	135	>150
Corner	56	123	>150	>>150

Table 5.11 Real Target Equivalent Velocities (mph) for the Steel-DU-Steel Truck Cask

Target/Orientation	Rigid Target Velocity			
	30 mph w/o limiter	60 mph w/o limiter	90 mph w/o limiter	120 mph w/o limiter
Soil				
End	>150	>>150	>>150	>>150
Side	99	>>150	>>150	>>150
Corner	128	>150	>>150	>>150
Concrete Slab				
End	134	>150	>150	>150
Side	56	142	>150	>>150
Corner	121	>150	>>150	>>150

Table 5.12 Real Target Equivalent Velocities (mph) for the Steel-Lead-Steel Rail Cask

Target/Orientation	Rigid Target Velocity			
	30 mph w/o limiter	60 mph w/o limiter	90 mph w/o limiter	120 mph w/o limiter
Soil				
End	>>150	>>150	>>150	>>150
Side	72	>150	>>150	>>150
Corner	68	133	>150	>150
Concrete Slab				
End	>150	>>150	>>150	>>150
Side	85	>150	>>150	>>150
Corner	>>150	>>150	>>150	>>150

Table 5.13 Real Target Equivalent Velocities (mph) for the Monolithic Steel Rail Cask

Target/Orientation	Rigid Target Velocity			
	30 mph w/o limiter	60 mph w/o limiter	90 mph w/o limiter	120 mph w/o limiter
Soil				
End	>150	>>150	>>150	>>150
Side	92	>150	>>150	>>150
Corner	111	>150	>>150	>>150
Concrete Slab				
End	>150	>>150	>>150	>>150
Side	104	>>150	>>150	>>150
Corner	>>150	>>150	>>150	>>150

5.2.8 Impacts onto Water

Equivalent velocities for impacts onto water targets for velocities greater than the regulatory impact are assumed to be above the range of possible impact velocities (150 mph). The incompressible nature of water makes perfectly flat impacts quite severe. As the impact velocity increases smaller deviations from the perfectly flat orientation are sufficient to cause the lack of shear strength in water to dominate the response. Because perfectly flat impacts are very improbable, this approach is justified.

5.2.9 Correlation of Results with Modal Study Event Trees

The Modal Study [5-12] event trees specify impact surfaces for each accident type. Because these event trees are used in this study to determine accident probabilities, this section will discuss which of the velocities determined above correlate to the surfaces specified in the event trees. For this study the event tree surface of railbed/roadbed will be treated as soil. The soil impacted in the tests used to calibrate the model was very hard desert soil, typical of Albuquerque, New Mexico. This soil is generally harder than the soil found on railbeds and roadbeds. For impacts onto the event tree surface of clay/silt the equivalent velocities will always be higher than the soil impact velocity derived here, but this velocity will be conservative and is therefore used. For the event tree surface of soft rock/hard rock/concrete the data from the concrete slab analyses will be used. In the Modal Study the equivalent velocities for the event tree surfaces of column and abutments were the same as those for the soft rock/hard soil/concrete surface. This approach will be repeated in this study. The event tree surface of hard rock will be treated as unyielding at all velocities, because the amount of energy absorbed by the rock is only a small portion of the impact energy. For all of the other impact surfaces the 30-mph equivalent velocity is taken directly from the Modal Study.

5.3 Puncture Analyses

Review of data from the Association of American Railroads (AAR) on the puncture of railroad tank cars indicates that cars with a shell thickness greater than or equal to one inch rarely experience puncture failures¹. Because the steel-lead-steel rail cask in this study has an outer shell thickness of two inches, it is highly unlikely that even the outer shell will be punctured in any rail accident. The containment boundary on the sandwich-wall casks is the inner shell, so puncture failure of the outer wall will not result in any release. The residual energy necessary to puncture the inner shell after the outer shell and shielding layers have been perforated is similar in magnitude to that required to puncture the outer shell, making loss of containment in puncture accidents even more unlikely. Figure 5.15 shows the relationship between tanker shell thickness and fraction of cars involved in puncture-type accidents that were failed because of puncture. Even the truck casks, which have thinner outer shells than rail casks, have a composite wall strength that is significantly greater than the strength of the strongest tank cars. The probability that these casks will be failed because of puncture is extremely low. This

1. Personal communication with D. J. Pasternak and data from RPI-AAR Railroad Tank Car Safety Research and Test Project, June 1998.

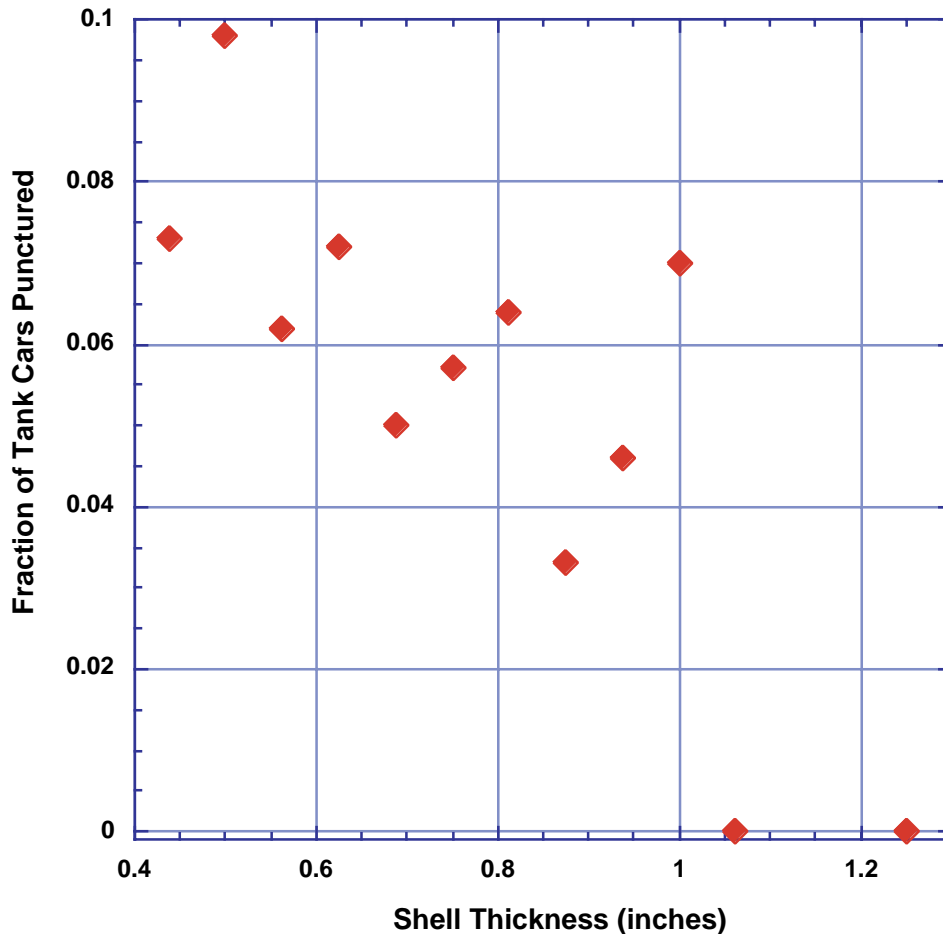


Figure 5.15 Fraction of railroad tank cars involved in puncture-type accidents that failed because of puncture.

is consistent with recent analyses performed by the NRC in response to questions from the AAR. These analyses concluded that it would be impossible for a rail coupler or a regulatory puncture spike to puncture the wall of a rail cask [5-16].

5.4 Failure of Rods

The percentage of fuel pins damaged for each impact is estimated based on the peak rigid-body acceleration. The STACE report [5-17] provides strains in the fuel pin cladding for a 100-G side impact for both PWR and BWR assemblies. In that report, it was shown that side impact provides the most severe loading to the fuel assemblies. During end-on impacts, the fuel assemblies are loaded by axial compressive loads. This type of loading will cause the individual rods to eventually buckle. Because of the limited space for lateral motion that results from this buckling and the very slender nature of the fuel rods, relatively low strains are produced. Therefore, in this report, the maximum strain generated in a fuel rod due to impacts onto a rigid target at any of the four speeds and three impact orientations modeled by the finite element calculations will be estimated using the peak acceleration of the impact to scale the largest strain generated in a fuel rod by a 100-G side impact. The rod will then be said to fail whenever the scaled strain level equals or exceeds the strain failure criterion developed in the next section.

5.4.1 Rod Failure Strain Criterion

As of 1994, the U.S. commercial spent fuel inventory contained about 49 percent low burnup (0 to 30 GWDt/MTU) fuel, about 49 percent intermediate burnup (30 to 45 GWDt/MTU) fuel, about 2 percent intermediate to high burnup (45 to 50 GWDt/MTU) fuel, and only 0.2 percent high burnup (50 to 60 GWDt/MTU) fuel [5-18]. Recent data suggest that, as of 1998, about 25 to 30 percent of PWRs and 15 to 20 percent of BWRs were producing high burnup fuel¹. Since hardly any high burnup fuel was being produced in 1994, linear extrapolation of this data suggests that by 2010 almost all U.S. commercial reactors will be producing high burnup spent fuel and about half will be producing high burnup fuel in 2002.

In 1994, the 109 power reactors that were operating in the United States generated 1883 MT of spent fuel [5-18] or 17.28 MT per reactor-year. If all of the U.S. commercial power reactors operating in 1999 extend their plant lives to 40 years, then data published in Nuclear News [5-19] allows the amounts of spent fuel that will be generated over the remaining life of these reactors to be calculated. The rate of conversion to high burnup fuel can be captured by assuming that from 1995 through 2001, all operating reactors will generate fuel with burnups of 40-45 GWDt/MTU and from 2002 through the end of their operating lives they will all generate high burnup fuel (fuel with burnups of 55-60 GWDt/MTU). Thus, during the seven year period from 1995 through 2001, 13181 MTU = (7 yrs)(1883 MTU per yr) of 40-45 GWDt/MTU fuel will be produced; and, after 2001, 33600 MTU = (17.28 MT per reactor)(1945 reactor-yr) of high burnup fuel will be produced where, as Table 5.14 shows, 1945 is the number of years of reactor operation after 2001 that will occur if all of the reactors operating in 1999 extend their plant lives to 40 years.

The strains that cause rod failure are expected to lie somewhere between the uniform plastic elongation (UE) and total plastic elongation (TE) strains that produce rod failure, probably well below the total elongation strains and not much above the uniform elongation strains². For average burnup fuel, the results of Bauer and Lowry [5-20] suggest that, when heated to 200 to 300° C, average burnup spent fuel will fail when UE strain levels reach 4 percent or TE strain levels reach 8 percent. For average burnup fuel, Sanders et al. [5-17] estimate that the probability of rod failure due to an impact that generates a biaxial stress ratio (pressurized fuel under tension) of 0.9 is 50 percent when the rupture strain is 4 percent. For high burnup fuel, the data of Smith et al. [5-21] and Garde et al. [5-22] indicate that at 300° C high burnup fuel will fail when UE strain levels reach 1 percent or TE strain levels reach 3.8 percent. Accordingly, 1 percent and 4 percent strains respectively are assumed to cause the cladding of high (55-60 GWDt/MTU) and high intermediate (40-45 GWDt/MTU) burnup spent fuel rods to fail, which suggests that the rod failure strain criterion will increase 1 percent for each 5 GWDt/MTU increase in burnup.

-
1. Personal communications, J. Finucane, Coal, Nuclear, and Renewable Fuels Division, U.S. Department of Energy, 1999.
 2. Personal communication, M. Billone, Argonne National Laboratory, 1999.

Table 5.14 Calculation of Reactor-Years Producing High Burnup Fuel

Reactor	Type	Start Year	Years >2001	Reactor	Type	Start Year	Years >2001	Reactor	Type	Start Year	Years >2001
Calloway	PWR	85	23	Arkansas 1	PWR	74	12	Hope Creek	BWR	86	24
Cook 1	PWR	75	13	Arkansas 2	PWR	80	18	Salem 1	PWR	77	15
Cook 2	PWR	78	16	Grand gulf	BWR	85	23	Salem 2	PWR	81	19
Palo Verde 1	PWR	86	24	River Bend	BWR	86	24	R.E. Ginna	PWR	70	8
Palo Verde 2	PWR	86	24	Waterford 3	BWR	85	23	Virgil C. Summer	PWR	84	22
Palo Verde 3	PWR	88	26	Davis Besse	PWR	78	16	South Texas 1	PWR	88	26
Calvert Cliffs 1	PWR	75	13	Perry 1	BWR	87	25	South Texas 2	PWR	89	27
Calvert Cliffs 2	PWR	77	15	St Lucie 1	PWR	76	14	San Onofre 2	PWR	83	21
Pilgrim	BWR	72	10	St Lucie 2	PWR	83	21	San Onofre 2	PWR	84	22
Brunswick 1	BWR	77	15	Turkey Point 1	PWR	72	10	Farley 1	PWR	77	15
Brunswick 2	BWR	75	13	Turkey Point 2	PWR	73	11	Farley 2	PWR	81	19
Robinson 2	PWR	71	9	Crystal River 3	PWR	77	15	Hatch 1	BWR	75	13
Shearon Harris	PWR	87	25	Oyster Creek	BWR	69	7	Hatch 2	BWR	79	17
Braidwood 1	PWR	88	26	Three Mile Island 1	PWR	74	12	Vogtle 1	PWR	87	25
Braidwood 2	PWR	88	26	Duane Arnold	BWR	75	13	Vogtle 2	PWR	89	27
Bryon 1	PWR	85	23	Clinton	BWR	87	25	Bellefonte1	PWR	95	33
Bryon 2	PWR	87	25	Cooper	BWR	74	12	Bellefonte2	PWR	95	33
Dresden 2	BWR	70	8	FitzPatrick	BWR	75	13	Browns Ferry 1	BWR	74	12
Dresden 3	BWR	71	9	Indian Point 3	PWR	76	14	Browns Ferry 2	BWR	75	13
LaSalle 1	BWR	84	22	Nine Mile Point 1	BWR	69	7	Browns Ferry 3	BWR	77	15
LaSalle 1	BWR	84	22	Nine Mile Point 1	BWR	88	26	Sequoyah 1	PWR	81	19
Quad Cities 1	BWR	73	11	Seabrook	PWR	90	28	Sequoyah 1	PWR	82	20
Quad Cities 2	BWR	73	11	Millstone 2	PWR	75	13	Watts Bar 1	PWR	96	34
Indian Point 2	PWR	74	12	Millstone 3	PWR	86	24	Watts Bar 2	PWR	95	33
Palisades	PWR	71	9	Monticello	BWR	71	9	Comanche Peak 1	PWR	90	28
Fermi 2	BWR	88	26	Prairie Island 1	PWR	73	11	Comanche Peak 2	PWR	93	31
Catawba 1	PWR	85	23	Prairie Island 2	PWR	74	12	Vermont Yankee	BWR	72	10
Catawba 2	PWR	86	24	Fort Calhoun	PWR	73	11	North Anna 1	PWR	78	16
McGuire 1	PWR	81	19	Susquehanna 1	BWR	83	21	North Anna 2	PWR	80	18
McGuire 2	PWR	84	22	Susquehanna 1	BWR	85	23	Surry 1	PWR	72	10
Oconee 1	PWR	73	11	Diablo Canyon 1	PWR	85	23	Surry 2	PWR	73	11
Oconee 2	PWR	74	12	Diablo Canyon 2	PWR	86	24	WPN-2	BWR	84	22
Oconee 3	PWR	74	12	Limerick 1	BWR	86	24	Point Beach 1	PWR	70	8
Beaver Valley 1	PWR	76	14	Limerick 2	BWR	90	28	Point Beach 2	PWR	72	10
Beaver Valley 2	PWR	87	25	Peach Bottom 1	BWR	74	12	Kewaunee	PWR	74	12
				Peach Bottom 2	BWR	74	12	Wolf Creek	PWR	85	23

Reactor-Years at High Burnup 1945

Use of the combination of the extrapolated amounts of intermediate and high burnup fuel with the 1994 data for metric tons of spent fuel by burnup range produces the basis for constructing an average strain failure level as a weighted sum of strain failure levels weighted by the amount of spent fuel in each burnup range. To do this, the cladding strains that produce rod failure are assumed to increase roughly linearly with decreasing fuel burnup. High burnup (55 to 60 GWDt/MTU) spent fuel is assumed to fail at 1 percent strain, intermediate burnup (40 to 45 GWDt/MTU) spent fuel fails at 4 percent strain, and low burnup (0 to 25 GWDt/MTU) spent fuel fails at 8 percent strain. As Table 5.15 shows, weighted summation of these cladding strain levels by burnup range produces an average failure strain level of 3.6 percent. This average is probably somewhat low for three reasons: (a) because it is derived using uniform elongation strains which are expected to underestimate somewhat the strains required to produce rod failure, (b) because not all operating reactors will extend their operating life to 40 years, and (c) because not all operating reactors will convert to a fuel management cycle that produces high burnup fuel. Accordingly, in agreement with the STACE report [5-17] and consistent with failure strains reported by Westinghouse for several burst tests [5-23], an average strain failure criterion of 4 percent seems reasonable for the U.S. commercial power reactor spent fuel inventory even after correcting for the amounts of high-burnup fuel likely to be produced during the remainder of the nuclear fuel cycle in the United States. Finally, a sensitivity calculation described below in Section 8.10.3, shows that, when rod failure fractions are set to 1.0 for all collision scenarios regardless of their severity, mean accident dose risks are increased by only a factor of 2.0. Thus, mean accident doses and dose risks are not particularly sensitive to the average value chosen for the strain criterion for rod failure during collision accidents.

Table 5.15 Calculation of Mass Weighted Sum of Burnup Dependent Rod Strain Failure Levels

GWDt per MTU	MTU	Criterion	
		Range	Weighted
0-25	8437	8	0.88
25-30	6177	7	0.56
30-35	6815	6	0.53
35-40	5149	5	0.34
40-45	2570	4	0.13
45-50	636	3	0.02
50-55	44	2	0.00
55-60	5	1	0.00
AvBU	13181	4	0.69
HBU	33600	1	0.44
Total	76614	Sum	3.60

5.4.2 Estimation of the Fraction of Rods Failed During Impacts

If the cladding strains are scaled by the ratio of peak rigid-body accelerations calculated in Section 5.2.2 to the 100-G acceleration used in the STACE report, the number of pins with cladding strains larger than 4 percent can be determined. These results are used to provide an estimate of fuel pin failure percentages. Table 5.16 gives the peak rigid-body accelerations for each of the analyses. Table 5.17 gives the strains in the fuel rods resulting from a 100-G impact, taken from Figures III-60 and III-64 of the STACE report. Scaling the strains in Table 5.17 by the accelerations in Table 5.16 and counting the number of rods with strains greater than 4 percent results in the fraction of rods failed given in Table 7.18 for each of the analyses.

Table 5.16 Peak Accelerations from Rigid Target Impacts without Impact Limiters, Gs

Cask	Orientation	30 mph	60 mph	90 mph	120 mph
Steel-Lead-Steel Truck	Corner	51.3	111.4	156.0	222.9
	End	200.6	289.8	378.9	445.8
	Side	127.0	312.1	490.4	757.8
Steel-DU-Steel Truck	Corner	132.6	224.3	291.6	346.7
	End	203.9	254.9	297.8	346.7
	Side	183.5	469.1	693.4	999.3
Steel-Lead-Steel Rail	Corner	50.6	94.4	145.9	n.a.
	End	167.3	303.0	371.1	483.6
	Side	73.3	178.8	349.7	n.a.
Monolithic Rail	Corner	93.8	174.2	259.1	335.1
	End	169.8	424.4	513.8	580.8
	Side	98.3	241.3	424.4	491.5

5.5 Conservatism in Calculating Structural Response

In this section the conservatism associated with the various assumptions in the determination of the structural response of the generic casks will be discussed in approximately the same order as the sections of this chapter.

Treating all corner impacts as if they were CG-over-corner forces all of the impact energy to be absorbed on the primary impact end. For corner impacts away from CG-over-corner, some of the initial kinetic energy of the cask will be converted into rotational kinetic energy at the end of the primary impact. This rotational kinetic energy will be absorbed by a secondary impact on the opposite end of the cask. Another conservatism in choosing the impact angles to be analyzed is the assumption that all end and corner impacts occur on the closure end of the cask. The deformations on the end away from the impact are much smaller, so if the impact occurs on the end away from the closure there will only be small deformations in the closure region and no releases for even the 120 mph impacts. In addition, the velocity vectors for all of the accidents are assumed to be perpendicular to the impact surface. In reality, there will be a distribution of angles between the velocity vector and the impact surface, and only the component of the

velocity vector that is perpendicular to the impact surface will cause damage to the cask. If the median of the distribution is at 45 degrees, this results in a 70% reduction, on average, in the component of velocity that produces damage.

Table 5.17 Peak Strains in Fuel Rods Resulting from a 100 G Impact

Fraction of PWR Rods	Peak Strain, %	Fraction of BWR Rods	Peak Strain, %
1/15	3.3	1/7	1.1
2/15	2.9	2/7	1
3/15	2.2	3/7	0.85
4/15	2	4/7	0.83
5/15	1.7	5/7	0.78
6/15	1.5	6/7	0.66
7/15	1.4	7/7	0.62
8/15	1.4		
9/15	1.4		
10/15	1.3		
11/15	1.3		
12/15	1.2		
13/15	1.2		
14/15	1.1		
15/15	1.1		

Treating the impact limiter material as completely locked-up from a 30-mph impact neglects the design margin that cask designers include in their impact limiter designs. For most cask designs the regulatory impact only uses about 50% of the energy absorbing capability of the impact limiter. If the impact limiter can absorb twice as much energy (the energy from a 60-foot free drop) the accident velocities associated with the 30, 60, 90 and 120 mph finite element calculations become 52, 73, 99, and 127 mph respectively instead of the 42, 67, 95, and 124 mph respectively used in this report.

The use of zero-thickness shell elements to represent the structural portions of the sandwich walls for the lead and DU shielded casks results in an overprediction of lead slump and strain in the walls. Because none of the walls had strains that were sufficiently high to indicate tearing of the stainless steel, the overprediction of these strains did not have any consequences. Therefore, the only consequence of the zero-thickness shells is for loss-of-shielding analyses.

Omitting the neutron shielding and any liner that is outside of it ignores the energy that will be absorbed by these components. During regulatory drops (30 mph) this is insignificant, but for higher velocity side impacts it is possible for the neutron shielding and its liner to absorb enough energy to reduce the damage to the remainder of the cask.

The seal leak path areas are only calculated at the location of one of the two o-rings typical in casks (the one that is closest to the interior of the cask). In reality, the o-rings at both locations can provide containment. For most of the analyses, the opening deflection at the location of the second o-ring is about half of the deflection at the inner o-ring.

The use of minimum material properties for the closure bolts results in a reduction of bolt clamping force and an over-estimation of bolt elongation. The specified bolt material (SA-540 Grade B23 Class 5) can have yield strengths more than 50% higher than the values used. Using more realistic values for bolt material parameters would result in smaller openings.

For soil impacts all of the results are based upon soil properties around Albuquerque, NM. This desert location has very hard soils (generally not tillable) compared to most of the rest of the nation. For impacts onto more typical soils even higher velocities would be required to obtain the damage levels from the rigid target finite element analyses. For impacts onto highway surfaces, all of the surfaces are assumed to be concrete. Impacts onto asphalt highway surfaces would be less severe. For impacts onto rock these analyses assumed the rock would absorb none of the impact energy. In reality, if a spent fuel cask were to impact into solid rock there would be some cracking and spalling of the rock surface as a result of the impact. This damage to the rock surface implies that it is absorbing some amount of energy.

Although the puncture data given in this chapter indicate the probability for puncturing a cask with a wall thickness greater than 1 inch is extremely remote, the risk analyses in this report assume the truck casks are punctured in 0.1% of the accidents. Even more conservative is the assumption that the rail casks are punctured in 1% of the rail-coupling impacts and 0.1% of all other impacts.

Scaling the strains in the spent fuel rods calculated for a 100 G impact by the accelerations for more severe impacts significantly overestimates the rod strains. As the geometry of a spent fuel assembly changes in the more severe impacts, the deformations become constrained due to limited space. Once this happens, the strains will no longer increase with increasing load.

5.6 References

- [5-1] L. M. Taylor and D. P. Flanagan, "PRONTO 3D, A Three-Dimensional Transient Solid Dynamics Program," SAND87-1912, Sandia National Laboratories, Albuquerque, NM, March 1989.
- [5-2] S. W. Attaway, "Update of PRONTO 2D and PRONTO 3D Transient Solid Dynamics Program," SAND90-0102, Sandia National Laboratories, Albuquerque, NM, November 1990.
- [5-3] V. L. Bergmann, "Transient Dynamics Analysis of Plates and Shells with PRONTO 3D," SAND91-1182, Sandia National Laboratories, Albuquerque, NM, September 1991.
- [5-4] J. S. Ludwigsen and D. J. Ammerman, "Analytical Determination of Package Response to Severe Impacts," Proceedings of PATRAM 95, Las Vegas, NV, December 1995.
- [5-5] D. J. Ammerman, "Benchmarking of Finite Element Codes for Radioactive Material Transportation Packages," in Development, Validation, and Application of Inelastic Methods for Structural Analysis and Design, PVP-Vol. 343, ASME, New York, NY, 1996.

- [5-6] D. J. Ammerman, "Effect of Closure Movement and O-ring Properties on Leak Rate," Contract report #239004, Sandia National Laboratories, Albuquerque, NM, September 1993.
- [5-7] G. W. Wellman and R. Salzbrenner, "Quasistatic Modeling and Testing of Exclusion Region Barrier Mock-Ups", SAND92-0024, Sandia National Laboratories, Albuquerque, New Mexico, March 1992.
- [5-8] American Society of Mechanical Engineers, "Specification for Alloy-Steel Bolting Materials for Special Applications," SA-540, ASME, New York, NY, 1998.
- [5-9] H. J. Rack and G. A. Knorovsky, "An Assessment of Stress-Strain Data Suitable for Finite-Element Elastic-Plastic Analysis of Shipping Containers," NUREG/CR-0481, SAND77-1872, Sandia National Laboratories, Albuquerque, NM, Sept. 1978.
- [5-10] M. K. Nielsen, H. S. Morgan, and R. D. Krieg, "A Phenomenological Constitutive Model for Low Density Polyurethane Foams," SAND86-2927, Sandia National Laboratories, Albuquerque, NM, April 1987.
- [5-11] Parker Seal Group, "Parker O-Ring Handbook," Parker Hannifin Corporation, Cleveland, OH, 1992, pp. A4-7.
- [5-12] L. E. Fisher, et al., "Shipping Container Response to Severe Highway and Railway Accident Conditions," NUREG/CR-4829, Lawrence Livermore National Laboratory, Livermore, CA, February 1987.
- [5-13] A. Gonzales, "Target Effects on Package Response: An Experimental and Analytical Evaluation," SAND86-2275, Sandia National Laboratories, Albuquerque, NM, May 1987.
- [5-14] I. G. Waddoups, "Air Drop Test of Shielded Radioactive Material Containers," SAND75-0276, Sandia National Laboratories, Albuquerque, NM, September 1975.
- [5-15] L. L. Bonzon and J. T. Schaumann, "Container Damage Correlation with Impact Velocity and Target Hardness," IAEA-SR-10/21, Transport Packaging for Radioactive Materials, IAEA, Vienna, Austria, 1976.
- [5-16] S. F. Shankman, Letter to R. E. Fronczak, Association of American Railroads – Responses to AAR's February 7, 1997 Questions, Nuclear Regulatory Commission, May 23, 1997.
- [5-17] T. L. Sanders, et al., "A Method for Determining the Spent-Fuel Contribution to Transport Cask Containment Requirements," SAND90-2406, Sandia National Laboratories, Albuquerque, NM, November 1992.
- [5-18] Spent Nuclear Fuel Discharges from U.S. Reactors, Energy Information Administration, U.S. Department of Energy, SR/CNEAF/96-01, 1994.

- [5-19] "World List of Nuclear Power Plants," *Nuclear News*, p. 52, March 1999.
- [5-20] A. A. Bauer and L. M. Lowry, *Nuclear Technology* **41**, 359 (1978).
- [5-21] G. P. Smith, et al., The Evaluation and Demonstration of Methods for Improved Nuclear Fuel Utilization, DOE.ET/34013-15, Combustion Engineering, Inc., Windsor, CT, 1994.
- [5-22] A. M. Garde, et al., "Effects of Hydride Precipitate Localization and Neutron Fluence on the Ductility of Irradiated Zircaloy-4," Zirconium in the Nuclear Industry: 11th International Symp., ASTM STP 1295, American Society for Testing and Materials, 1996, p. 407.
- [5-23] M. G. Balfour, et al., "Final Report, EP80-16, Hot Cell Examination of Zion Fuel Cycles 1 Through 4," WCAP-10473, Westinghouse Energy Systems, Pittsburgh PA 15230, April 1985.

This page intentionally left blank.